PAPER

Check for updates

Zn₃V₂O₇(OH)₂·2H₂O/MXene cathode with fast ion diffusion for highly durable zinc ion batteries†

Wanting Su,‡ Man Lang,‡ Weiwei Li and Huili Li 🄳 *

V-based materials are considered promising candidates as cathode materials for zinc ion batteries (ZIBs). However, the inherent low conductivity of V-based compounds leads to the sluggish diffusion kinetics of Zn^{2+} and serious cycling capacity degradation of ZIBs. Herein, 1D $Zn_3V_2O_7(OH)_2 \cdot 2H_2O$ (ZVO) nanowires were grown on monodisperse 2D $Ti_3C_2T_x$ MXene nanosheets *via* a facile microwave-assisted method. The introduction of $Ti_3C_2T_x$ MXenes effectively improved the conductivity and hydrophilicity of ZVO. Furthermore, the Zn^{2+} diffusion coefficient of ZVO/$Ti_3C_2T_x$ composites was enhanced to 10^{-7}–10^{-8} cm² s⁻¹, which was superior to that of pure ZVO nanowires (10^{-8}–10^{-10} cm² s⁻¹) and other previously reported typical V-based cathodes. The ZIBs based on the ZVO/$Ti_3C_2T_x$ cathode possessed an excellent discharge specific capacity of 215.2 mAh g⁻¹ at 0.1 A g⁻¹ and cycling stability (84% retention over 14 000 cycles at 10 A g⁻¹). Moreover, the flexible Zn//ZVO/$Ti_3C_2T_x$ ZIBs using a gel electrolyte still exhibited good cycling stability and rate performance.

Introduction

Recently, cost-effective, environmentally friendly energy storage materials with high capacity and long life have attracted increasing attention.[1,2] Li-ion batteries face intrinsic safety issues caused by hazardous and flammable organic electrolytes and have high production cost.[3,4] Extensive research has been conducted on metal-ion batteries (Mg^{2+}, Zn^{2+}, Na^+, *etc.*) with eco-friendly aqueous electrolytes, which are abundant in resources and inexpensive.[5–8] Particularly, aqueous zinc ion batteries (ZIBs) have attracted more attention owing to the chemical and physical properties of the zinc anode, including low redox potential (−0.763 V *vs.* standard hydrogen electrode), high theoretical specific capacity (820 mAh g⁻¹ and 5855 mAh cm⁻³), environmental friendliness and high safety characteristics.[9,10] In view of the most significant component, cathodes, such as manganese-based compounds, V-based compounds, organic substances and Prussian blue analogs, have been extensively developed.[11–13] V-based materials are promising candidates for ZIB cathode materials owing to their low cost, multi-valence states (V^{3+}, V^{4+}, V^{5+}), and large interlayer/tunnel spacing.[14–16]

Typically, $Zn_3V_2O_7(OH)_2 \cdot 2H_2O$ (ZVO) with a layered octahedron and columnar hexahedron structure has become

a powerful competitor with improved electron migration and high Zn^{2+} storage capacity for ZIBs.[17] ZVO nanowires were first synthesized using a microwave-assisted method and used as cathodes for ZIBs.[18] Zn//ZVO batteries showed about a 68% retention ratio of original discharge capacity after 300 cycles at 0.2 A g⁻¹. The diffusion coefficient of Zn^{2+} ions was approximately 10^{-9}–10^{-10} cm² s⁻¹. ZVO nanowires with exposed (001) plane lattice exhibited a specific discharge capacity of 108 mAh g⁻¹ (about 77% retention) after 700 cycles at 2 A g⁻¹ and a diffusion coefficient of 10^{-11}–10^{-10} cm² s⁻¹ for the Zn^{2+} ion.[19] Few modification methods have been proposed to improve the diffusion kinetics of Zn^{2+} and cycling capacity of ZVO-based ZIBs.[20,21] Conductive and flexible current collectors such as 1D carbon nanotubes and carbon cloth were used to improve the electrochemical reaction kinetics of ZVO, which facilitated Zn^{2+} diffusion and accelerated electron transport.[22–24] An ultrathin HfO_2 film was coated on ZVO as an artificial solid electrolyte interphase to decrease the by-product and suppress the dissolution of the ZVO cathode. The obtained HfO_2-coated ZVO cathodes delivered 90% retention over 100 cycles at 0.1 A g⁻¹ and 84% retention over 1000 cycles at 10 A g⁻¹.[25] In addition, the diffusion coefficient of Zn^{2+} was improved to 5×10^{-8}–6.9×10^{-8} cm² s⁻¹ by constructing the bridge oxygen vacancies for refined 1D Zn^{2+} ion transport channels in ZVO.[26] Gradient concentration of N was refilled into partial oxygen vacancies to further enhance the stability of oxygen vacancies and reduce the energy barrier for Zn^{2+} diffusion.[27] Nonetheless, some issues, such as low inherent conductivity and poor structural stability, still need to be further improved.

Herein, ZVO/$Ti_3C_2T_x$ composites were synthesized by growing 1D ZVO nanowires on the monodisperse 2D MXene by

The Education Ministry Key Lab of Resource Chemistry, Shanghai Key Laboratory of Rare Earth Functional Materials, College of Chemistry and Materials Science, Shanghai Normal University, Shanghai 200234, P. R. China. E-mail: li_huili@shnu.edu.cn

‡ Wanting Su and Man Lang contributed equally to this work.

a facile microwave-assisted method. The MXene as the conductive and hydrophilic substrate additive not only provided abundant reactive sites but also enhanced the hydrophilicity and structural stability of $ZVO/Ti_3C_2T_x$ composites. Moreover, the diffusion coefficient of Zn^{2+} and electrolyte-philicity of $ZVO/Ti_3C_2T_x$ composites were significantly improved. The $ZVO/Ti_3C_2T_x$ composites exhibited high discharge capacities of about 215.2 mAh g^{-1} at a current density of 0.1 A g^{-1}. Impressively, the as-fabricated $ZVO/Ti_3C_2T_x$ cathodes remained at about 84% and 88% capacity retention after 14 000 cycles at 10 A g^{-1} and 1200 cycles at 2 A g^{-1}, respectively. Furthermore, the cycle stability and rate performance of $ZVO/Ti_3C_2T_x$ cathode ZIBs constructed by gel electrolyte were demonstrated.

Experimental

Synthesis of $Ti_3C_2T_x$

$Ti_3C_2T_x$ was achieved through selective etching of the Al layer from Ti_3AlC_2 feedstock. First, 3.2 g LiF was dissolved in 40 mL 9 mol L^{-1} HCl to obtain a homogeneous solution, followed by gradually adding Ti_3AlC_2. Next, the above mixture was stirred for 24 hours at 35 °C. Then, the obtained solution was washed with deionized water by centrifugation until the pH of the supernatant reached approximately 6, which was followed by sonication for 1 hour in an argon environment. Finally, the resulting solution was subsequently centrifuged at 3500 rpm for 20 minutes to obtain a specific concentration of $Ti_3C_2T_x$ dispersion.

Synthesis of $Zn_3V_2O_7(OH)_2\cdot 2H_2O/Ti_3C_2T_x$ composites

Firstly, 1 mmol ammonium metavanadate (NH_4VO_3) was dissolved in 10 mL deionized water with stirring at 80 °C. Then, 1.5 mmol zinc nitrate hexahydrate ($Zn(NO_3)_2\cdot 6H_2O$) dissolved in 10 mL deionized water and $Ti_3C_2T_x$ were orderly poured into the NH_4VO_3 solution. Finally, the mixed solution was transferred into a microwave reaction tube and reacted at 160 °C for 6 h. The resulting $ZVO/Ti_3C_2T_x$ composites were washed with deionized water, followed by freeze-drying for later application. In contrast, ZVO nanowires were synthesized without the addition of $Ti_3C_2T_x$.

The assembling of the zinc-ion batteries

The $ZVO/Ti_3C_2T_x$ cathode was prepared by mixing the active material and conductive carbon black (Super P) and polyvinylidene fluoride (PVDF) binder in a ratio of 7 : 2 : 1. The mixture was vigorously stirred for 12 h, and then the resulting slurry was uniformly coated on a titanium foil substrate. The coated substrate was vacuum-dried at 80 °C for 12 h, followed by cutting into circular pieces. The average loading of the active material on the prepared cathode was 1.0–1.5 mg cm^{-2}. The ZIB was built in a CR2032 coin cell with $ZVO/Ti_3C_2T_x$ cathode, zinc foil anode, along with 21 mol L^{-1} lithium bis(trifluoromethanesulfonyl)imide (LiTFSI) and 1 mol L^{-1} zinc trifluoromethanesulfonate ($Zn(CF_3SO_3)_2$) solution and a glass fiber filter membrane, which were respectively used as the electrolyte and the septum.

The assembling of the flexible zinc-ion batteries

First, 3.02 g LiTFSI and 0.18 g $Zn(CF_3SO_3)_2$ were completely dissolved in 0.5 mL deionized water. Then, 160 mg acrylamide (AM), 3 mg ammonium persulfate (APS), and 0.15 mg N,N'-methylenebisacrylamide (MBA) were added to the above solution under stirring. Finally, the mixtures were injected into a mold, followed by heating at 70 °C for 1.5 h to obtain the polyacrylamide (PAM) hydrogel. The flexible zinc-ion batteries were assembled using the sandwich-type structure, where the $ZVO/Ti_3C_2T_x$ electrodes and zinc electrodes were directly attached to the sides of the PAM hydrogel.

Characterization

Field emission scanning electron microscopy (SEM, HITACHI, S–4800) and transmission electron microscopy (TEM, JEOL JEM–2100) were performed to observe the morphology and microstructure of the samples. X-ray powder diffraction (XRD) and X-ray photoelectron spectroscopy (XPS) were respectively observed using Rigaku D/Max B diffractometer with Cu Kα radiation and Thermo Scientific Nexsa system. The Electrochemical characterizations were carried out using the LAND 2001A cell test system and electrochemical workstation (CHI 760E).

Results and discussion

Synthesis and characterization of $Zn_3V_2O_7(OH)_2\cdot 2H_2O/Ti_3C_2T_x$ composites

The $ZVO/Ti_3C_2T_x$ composites were constructed by growing ZVO on the single-layer $Ti_3C_2T_x$ nanosheets, as shown in Fig. 1a. Firstly, the single-layer dispersed $Ti_3C_2T_x$ MXenes were obtained by etching the Al layer of Ti_3AlC_2 MAX using LiF and HCl, followed by an ultrasonic process. Before etching, Ti_3AlC_2 MAX appeared as a tightly packed and multilayered block (Fig. S1†). The XRD spectrum showed that the (002) characteristic peak of Ti_3AlC_2 MAX shifted from 9.6° to 6.7° after etching, indicating the successful preparation of $Ti_3C_2T_x$ MXene with increased interlayer spacing (Fig. S2†). Subsequently, multiple layers of $Ti_3C_2T_x$ were subjected to ultrasonic treatment, resulting in uniform single-layer MXene dispersion (Fig. S3†) with a thickness of 1.5 nm (Fig. S4†). The ZVO nanowires of $ZVO/Ti_3C_2T_x$ composites were synthesized by a microwave-assisted method of $Zn(NO_3)_2\cdot 6H_2O$ and NH_4VO_3 in $Ti_3C_2T_x$ (Fig. S5†). The capacity and cycling stability of $ZVO/Ti_3C_2T_x$ composites were systematically adjusted by changing the chemical concentrations, reaction temperature, reaction time and MXene weight (Fig. S6–S9†). According to the XRD spectrum, the distinct characteristic diffraction peaks observed at 12.5°, 17.1°, 21.2°, 30.3°, 32.2°, 34.4° and 36.7° correspond to the (001), (010), (011), (012), (111), (020), and (021) crystal planes of ZVO (Fig. 1b). All peaks were consistent with the standard card PDF#50-0570 of hexagonal ZVO, indicating the successful synthesis of $ZVO/Ti_3C_2T_x$ composites.

XPS spectra were conducted for the chemical composition and valence state of $ZVO/Ti_3C_2T_x$ MXene composites. Obviously, the elements C, Ti, V, O, and Zn were confirmed in the ZVO/
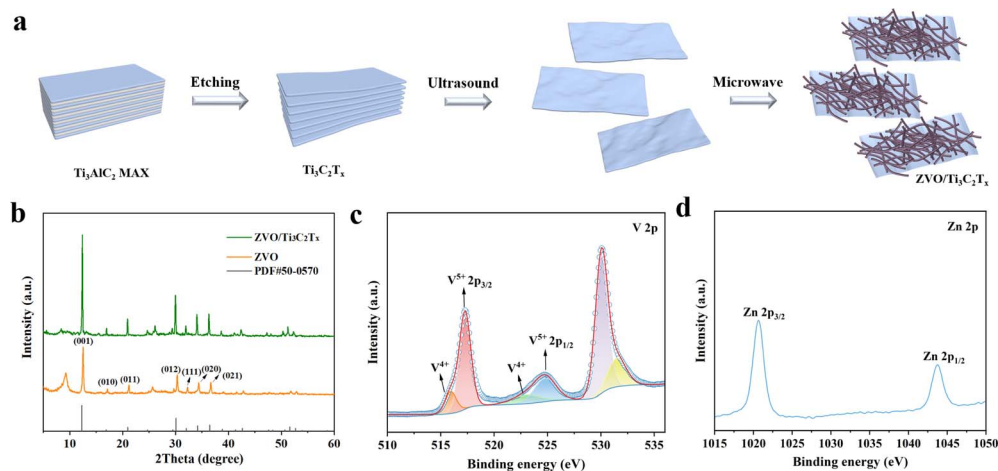
Fig. 1 (a) Schematic synthesis of ZVO/Ti$_3$C$_2$T$_x$ composites. (b) XRD patterns of ZVO and ZVO/Ti$_3$C$_2$T$_x$ composites. The high-resolution XPS spectrum of (c) V 2p and (d) Zn 2p in the ZVO/Ti$_3$C$_2$T$_x$ composites.†

Ti$_3$C$_2$T$_x$ composites (Fig. S10†). As shown in the high-resolution XPS spectrum (Fig. 1c), the strong peaks at 517.3 eV and 524.9 eV were attributed to V^{5+} 2p$_{3/2}$ and V^{5+} 2p$_{1/2}$, respectively. Moreover, the characteristic peak of V^{4+} appeared as broad peaks at 515.9 eV and 523.18 eV. V in the hierarchical structure of ZVO/Ti$_3$C$_2$T$_x$ MXene composite was dominant in the oxidization of V^{5+} and minimal in V^{4+}. In the high-resolution Zn 2p spectrum (Fig. 1d), two distinct characteristic peaks at binding energies of 1020.7 eV and 1043.8 eV, mainly ascribed to the 2p$_{3/2}$ and 2p$_{1/2}$ of Zn in the ZVO/Ti$_3$C$_2$T$_x$ composite, respectively. The characteristic absorption peak of the M−O bond appeared at 530.1 eV, mainly reflecting the bond between the metal atoms (Zn or V) and oxygen atoms, as shown in Fig. S10b.† Additionally, the absorption peak at binding energies of 531.4 eV was ascribed to the characteristic peak of the C–O bond.

The morphology and structure of ZVO and ZVO/Ti$_3$C$_2$T$_x$ composites were investigated through SEM, EDX, and TEM analyses. As shown in Fig. S11,† the prepared ZVO exhibited interweaved and stacked nanowire morphology. After the introduction of Ti$_3$C$_2$T$_x$, ZVO nanowires were tightly wrapped around the two-dimensional Ti$_3$C$_2$T$_x$ layer, as shown in Fig. 2a and S12†. Moreover, the self-aggregation of ZVO nanowires was prevented, attributing to the two-dimensional Ti$_3$C$_2$T$_x$, resulting in better electrochemical properties. Similar to the SEM images, the fabricated ZVO nanowires manufactured on the ZVO/Ti$_3$C$_2$T$_x$ composite were elucidated with an interlayer spacing of 0.72 nm (Fig. 2b, c and S13†), which is consistent with the XRD results (Fig. 1b). Furthermore, V, O, Zn, and Ti elements were uniformly distributed on the ZVO/Ti$_3$C$_2$T$_x$ composites, as shown in Fig. 2d.

Electrochemical performance of zinc-ion batteries

To determine the electrochemical performance of the ZVO/Ti$_3$C$_2$T$_x$ composite, Zn//ZVO/Ti$_3$C$_2$T$_x$ ZIBs were fabricated by

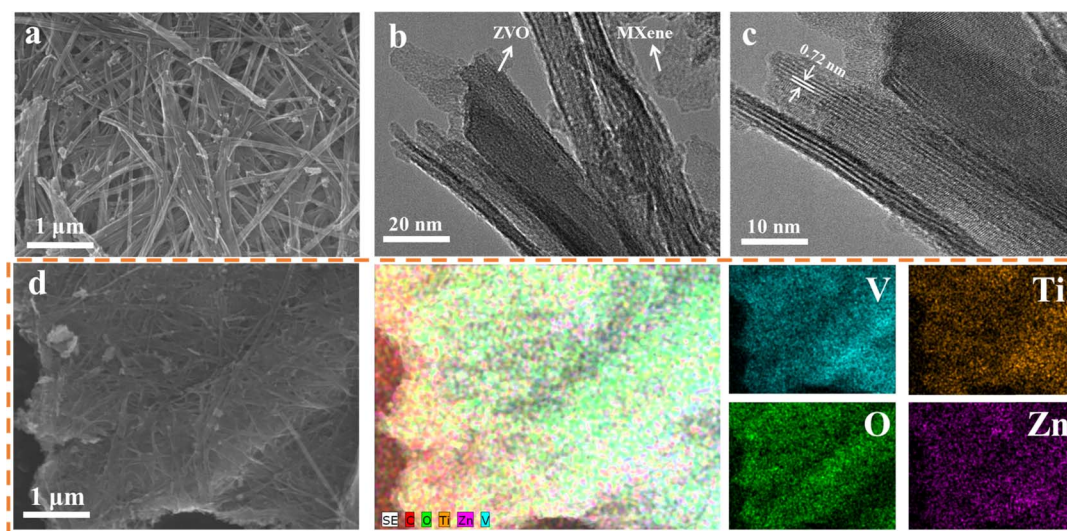**Fig. 2** (a) SEM image and (b and c) TEM images and (d) element mapping of ZVO/Ti$_3$C$_2$T$_x$ composites.

utilizing a 21 mol L^{-1} LiTFSI + 1 mol L^{-1} Zn(CF$_3$SO$_3$)$_2$ electrolyte, zinc foil anode, and ZVO/Ti$_3$C$_2$T$_x$ cathode (Fig. 3a). Galvanostatic charge/discharge (GCD) curves and rate capability of Zn//ZVO/Ti$_3$C$_2$T$_x$ batteries were examined between 0 V and 1.8 V under various current densities, as shown in Fig. 3b and c. The Zn//ZVO/Ti$_3$C$_2$T$_x$ battery exhibited a discharge capacity of 215.2 mAh g^{-1} at a current density of 0.1 A g^{-1} (Fig. 3b). Upon increasing current densities from 0.2, 0.5, and 1.0, to 2.0 A g^{-1}, the discharge capacities were 185.8, 155.5, 129.1 and 95.2 mAh g^{-1}, respectively, which were comparable to those of other reported vanadium-based ZIBs (Fig. S14†).[18,25,28–35] In addition, when the current density returned to 0.1 A g^{-1}, the discharge capacity of Zn//ZVO/Ti$_3$C$_2$T$_x$ batteries reached 209.9 mAh g^{-1}, retaining about 98% of the original discharge capacity (Fig. 3c). This indicated that the prepared Zn//ZVO/Ti$_3$C$_2$T$_x$ batteries exhibited good rate performance and specific discharge capacities, better than that of pure ZVO (Fig. S15†). The results showed that the introduction of 2D Ti$_3$C$_2$T$_x$ nanosheets with a high specific surface area can effectively increase the specific surface area of the ZVO/Ti$_3$C$_2$T$_x$ composites, resulting in the increased number of active sites for the reaction between the Zn^{2+} and ZVO/Ti$_3$C$_2$T$_x$ cathode (Fig. S16†). The reaction kinetics of Zn^{2+} and conductivity of ZVO/Ti$_3$C$_2$T$_x$ cathode were respectively speeded up and improved due to the high conductivity of Ti$_3$C$_2$T$_x$ (Fig. S17†), resulting in smaller charge transfer resistance (R_{ct}, Fig. 3d). Furthermore, the introduction of Ti$_3$C$_2$T$_x$ containing abundant hydrophilic groups has been found to effectively improve the hydrophilicity of the ZVO/Ti$_3$C$_2$T$_x$ cathode with electrolyte (Fig. S18†). As a result, the internal ion migration resistance of the electrode was reduced, enabling a complete reaction between Zn^{2+} in the electrolyte and the electrode material. Furthermore, this increase in hydrophilicity accelerated the diffusion rate of ions

with lower ion diffusion resistance (Z_w, Fig. 3d). The addition of highly conductive MXene effectively decreased the charge transfer resistance (R_{ct}) of the ZVO/Ti$_3$C$_2$T$_x$ cathode, indicating the promotion of electronic conductivity than that of ZVO. As shown in Fig. 3d, the impedance data were analyzed and fitted to a typical equivalent electrical circuit consisting of the series resistance (R_s), interface resistance (R_i), constant-phase element (CPE), R_{ct} and Warburg diffusion behavior (W). In addition, Zn//ZVO/Ti$_3$C$_2$T$_x$ ZIBs exhibited a power density of 1220 W kg^{-1} and an energy density of 141.6 W h kg^{-1}.

To further investigate the effect of the introduction of 2D Ti$_3$C$_2$T$_x$, the cycling performance of the battery was tested at 2 A g^{-1}. The discharge specific capacity of Zn//ZVO/Ti$_3$C$_2$T$_x$ batteries could maintain 88% of initial capacity after 1200 charge/discharge cycles (Fig. 3e). The local damage of the ZVO/Ti$_3$C$_2$T$_x$ structure led to a weakened intensity of the (001) characteristic peak (Fig. S19a†) and increased charge transfer resistance (Fig. S19b†) after cycling, resulting in slightly decreased discharge specific capacities. In contrast, the capacity of Zn//ZVO batteries decreased rapidly, retaining only 38% of the initial capacity. Especially, Zn//ZVO/Ti$_3$C$_2$T$_x$ batteries could still retain 84% of initial capacity after 14 000 cycles at a large current density of 10.0 A g^{-1} (Fig. 3f), even maintaining 95% after 60 cycles at a low current density of 0.1 A g^{-1} (Fig. S20†). The cycling performance of the Zn//ZVO/Ti$_3$C$_2$T$_x$ battery was superior to most other previously reported vanadium-based cathodes (Table S1†).[18–23,25,36–39] That was because the introduction of Ti$_3$C$_2$T$_x$ effectively inhibited the self-stacking of ZVO nanowires and mitigated the structural damage during Zn^{2+} intercalation/deintercalation. To explore the practical application value of ZIBs, two ZIBs connected in series can be used to power a clock (Fig. S21†). This demonstrated that the prepared ZIBs can be utilized as electrochemical storage devices for other electronic products.
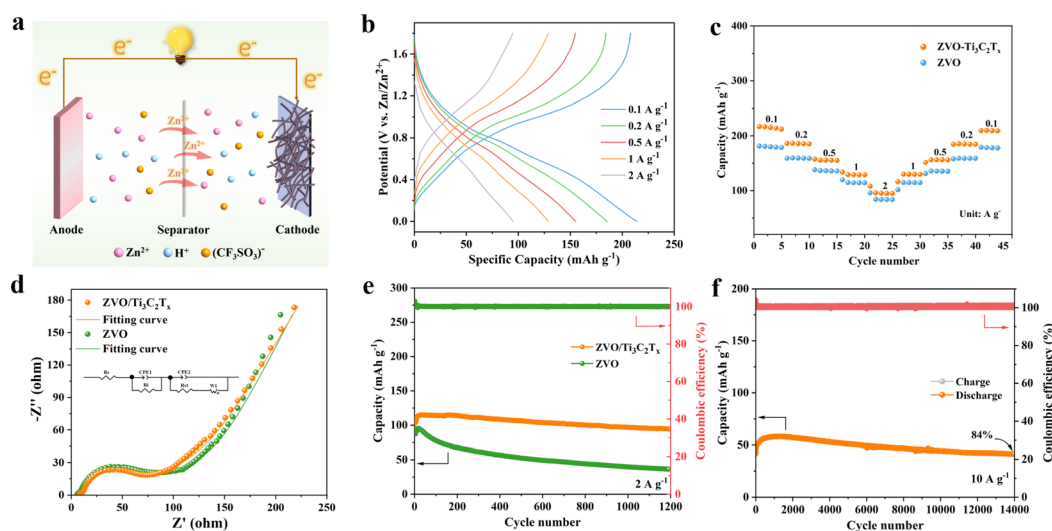

Fig. 3 Electrochemical performances of Zn//ZVO/Ti$_3$C$_2$T$_x$ batteries in 21 mol L^{-1} LiTFSI + 1 mol L^{-1} Zn(CF$_3$SO$_3$)$_2$ aqueous electrolyte. (a) Schematic of the mechanism of the Zn//ZVO/Ti$_3$C$_2$T$_x$ battery. (b) The galvanotactic charge/discharge curves and (c) rate capability of Zn//ZVO/Ti$_3$C$_2$T$_x$ batteries under different current densities. (d) Electrochemical impedance spectroscopy (EIS) spectra of Zn//ZVO/Ti$_3$C$_2$T$_x$ and Zn//ZVO batteries. Inset: the partial enlargement of the EIS spectra at the high-frequency region. Long cycling performance of Zn//ZVO/Ti$_3$C$_2$T$_x$ batteries at (e) 2 A g^{-1} and (f) 10 A g^{-1}.

Kinetics of zinc-ion batteries

Cyclic voltammogram (CV) measurements were performed further to confirm the kinetics performance of Zn//ZVO/Ti$_3$C$_2$T$_x$ batteries. It can be observed that the CV curves almost overlapped, indicating the stable redox potential and highly reversible electrochemical transformation of the ZVO/Ti$_3$C$_2$T$_x$ cathode (Fig. S22†). In addition, the area of the CV curve gradually increased with the increase in scanning rate from 0.2 mV s^{-1} to 1.0 mV s^{-1}, as well as a lower cathodic and a higher anodic peak shift simultaneously (Fig. 4a). Two pairs of redox peaks were located at 0.49 V/0.76 V and 0.75 V/1.10 V at 0.2 mV s^{-1}, consistent with the redox discharge and charge platforms in the previously tested GCD curve (Fig. 3b). The mentioned cathodic and anode peaks corresponded to the insertion/desertion of zinc ions, respectively.

To better understand the afore-mentioned superior performance, the power-law relationship between the peak current (i) and scan rate (v) can be determined by the following equation:

$$i = av^b$$

a and b were variable parameters in the formula. In general, the coefficient b varied in the range of 0.5 to 1.0, reflecting the rate-limiting step and different charge storage states. The discharge/charge process was completely dominated by the ionic diffusion-controlled process ($b = 0.5$) while attributed to the capacitive-limited behavior through a fast surface reaction ($b = 1.0$). According to the fitting curve in Fig. 4b, the b values fitted to the four peaks of Zn//ZVO/Ti$_3$C$_2$T$_x$ batteries were respectively calculated as 0.73, 0.68, 0.70 and 0.68, indicating the co-dominated discharge/charge process by capacitive behavior and ionic diffusion-controlled process. The following deformed equation was further used to accurately determine the

contribution ratios of capacitive-limited behavior and diffusion-controlled process:

$$i = k_1 v + k_2 v^{1/2}$$

where k_1 and k_2 were varied parameters with the peak current (i). Generally, $k_1 v$ and $k_2 v^{1/2}$ represented the capacitive-limited and ionic diffusion-controlled contribution of the total capacity, respectively. At the scanning speed of 0.4 mV s^{-1}, the capacitive contribution rate was about 61.3% of the overall capacity (Fig. 4c). Fig. 4d demonstrates the ratio of capacitive-limited contribution (orange) and ionic diffusion-controlled contribution (green) as a function of scan rate. The capacitive-limited contribution gradually increased from 53.7% to 75.2% with the increase in the scanning rate from 0.2 to 1.0 mV s^{-1}. The capacitance contribution rates of Zn//ZVO/Ti$_3$C$_2$T$_x$ batteries were larger than those of Zn//ZVO batteries at the same scanning rate (Fig. S23†). This was because of the increasing active sites of the Zn^{2+} reaction with a larger specific surface area and more electrolyte-philic cathode due to the introduction of Ti$_3$C$_2$T$_x$ and a small capacitance of Ti$_3$C$_2$T$_x$.

The galvanostatic intermittent titration technique (GITT) was further demonstrated to investigate the Zn^{2+} kinetics diffusion behavior in the lattices of ZVO/Ti$_3$C$_2$T$_x$ composite cathodes. The diffusion coefficient of Zn^{2+} ($D_{Zn^{2+}}$) was determined using the following formula:

$$D_{Zn^{2+}} = \frac{4}{\pi \tau} \left(\frac{m V_m}{MA} \right)^2 \left(\frac{\Delta E_s}{\Delta E_\tau} \right)^2$$

τ, M, m, V_m, and A represent the relaxation time, molar mass of active materials, mass of active materials, molar volume, and effective contact area between the electrode and electrolyte,
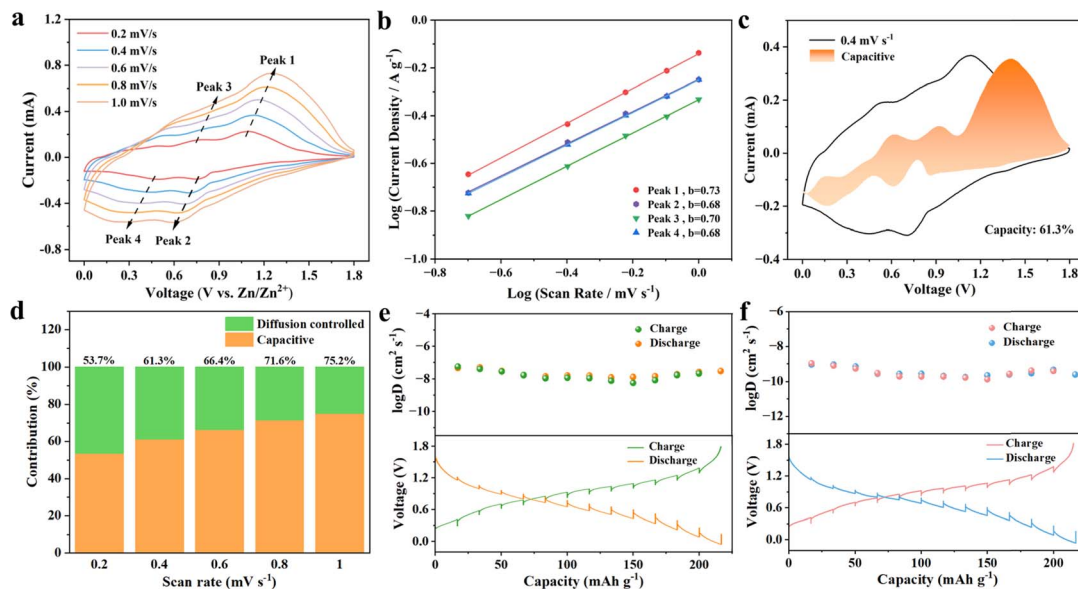

Fig. 4 (a) Cyclic voltammogram profiles of Zn//ZVO/Ti$_3$C$_2$T$_x$ batteries at different scan rates. (b) The fitting plots between log (i) and log (v) at different peak currents. (c) Quantification of the capacitive (orange area) and diffusion charge storage in the ZVO/Ti$_3$C$_2$T$_x$ electrode at a scan rate of 0.4 mV s^{-1} and (d) the ratio of the capacitive contribution (orange) to the diffusion contribution (green) as a function of scan rate. GITT curves and corresponding Zn^{2+} diffusion coefficients for (e) Zn//ZVO/Ti$_3$C$_2$T$_x$ batteries and (f) Zn//ZVO batteries at 0.5 A g^{-1}.

respectively. Especially, ΔE_s and ΔE_τ were the voltage change of pulse and voltage change of constant-current charge/discharge, respectively. GITT curves and the corresponding $D_{Zn^{2+}}$ of Zn// ZVO/Ti$_3$C$_2$T$_x$ batteries and Zn//ZVO batteries at 0.5 A g^{-1} are shown in Fig. 4e and f. The Zn^{2+} diffusion coefficient of ZVO/ Ti$_3$C$_2$T$_x$ composites as the cathode was calculated in the range of 10^{-7} to 10^{-8} cm^2 s^{-1}, which was superior to pure ZVO nanowires (10^{-8}–10^{-10} cm^2 s^{-1}) and other previously reported typical vanadium-based cathodes.[20,36,40–44] The introduction of Ti$_3$C$_2$T$_x$ with high electrical conductivity and good hydrophilic properties inhibited the self-stacking of ZVO nanowires and increased available active areas, resulting in fast solid-state diffusion kinetics of Zn^{2+}. This also accounted for the superior cycling performances and rate properties of the Zn//ZVO/ Ti$_3$C$_2$T$_x$ battery.

Mechanism of zinc-ion batteries

In order to further study the zinc storage mechanism of ZVO/ Ti$_3$C$_2$T$_x$ electrodes, *ex situ* XRD and XPS characterization were conducted. Various charge/discharge states (points A–G) were subjected to *ex situ* XRD analysis at 0.5 A g^{-1}, as shown in Fig. 5a and b. When discharging from 1.8 V to 0 V, the 2θ angle shifted from 12.1° at point A to 11.8° at point D. This shift indicated that Zn^{2+} ions were inserted into the ZVO/Ti$_3$C$_2$T$_x$ layers during discharge, causing an expansion of the interlayer spacing. Upon

charging back to 1.8 V, the (001) peak position of ZVO/Ti$_3$C$_2$T$_x$ almost returned to its starting position at point A, ascribing to the desertion of Zn^{2+} from ZVO/Ti$_3$C$_2$T$_x$. The well-designed ZVO/ Ti$_3$C$_2$T$_x$ represented high reversibility of Zn^{2+} intercalation/ deintercalation.

The reversible insertion/desertion mechanism of Zn^{2+} was further verified using *ex situ* XPS, as shown in Fig. 5c–e. In the fully charged states A (Fig. 5c), two remarkable diffraction peaks that corresponded to Zn 2p$_{1/2}$ and Zn 2p$_{3/2}$ were observed at 1022.1 eV and 1045.1 eV, which were detected in the Zn 2p fine XPS spectra of the original ZVO/Ti$_3$C$_2$T$_x$ composites (Fig. 1d). When discharged to 0 V (at point D, Fig. 5d), new peaks from the Zn 2p$_{3/2}$ and Zn 2p$_{1/2}$ orbitals appeared at 1021.3 eV and 1044.1 eV, respectively, indicating the successful insertion of Zn^{2+} from the electrolyte into the ZVO/Ti$_3$C$_2$T$_x$ electrode. Upon charging back to G (1.8 V, Fig. 5e), new peaks from Zn 2p$_{3/2}$ and Zn 2p$_{1/2}$ disappeared, while XPS spectroscopy of Zn 2p returned to its starting position at point A. The effect of Zn^{2+} on the valence changes of V elements can be evidenced in the *ex situ* XPS patterns (Fig. 5c–e). When discharging to 0 V, the intensity of V^{5+} weakened and another V 2p$_{3/2}$ feature appeared, indicating a partial reduction of V^{5+} to V$^{\delta+}$ ($4 < \delta < 5$). At the fully charged state of A or G, the V$^{\delta+}$ contribution almost diminished. These results confirmed the zinc storage mechanism of the ZVO/Ti$_3$C$_2$T$_x$ electrode consistent with the *ex situ* XRD results (Fig. 5b), indicating good reversibility and stability of the ZVO/Ti$_3$C$_2$T$_x$ electrode.
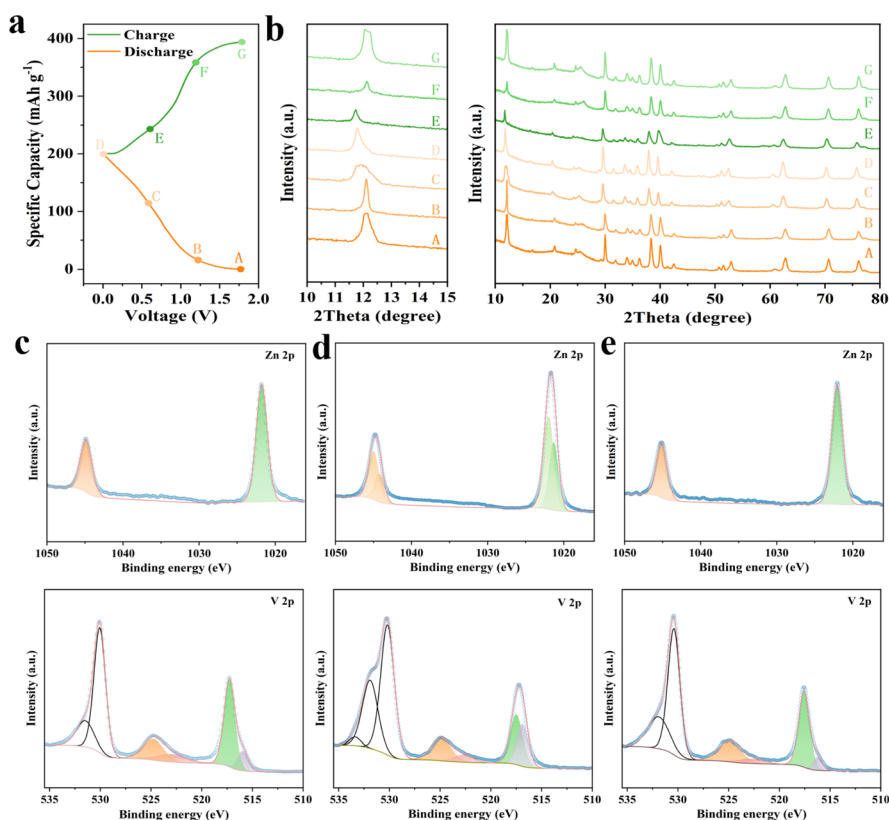

Fig. 5 Zn-storage mechanism of ZVO/Ti$_3$C$_2$T$_x$ composites. (a) Charge/discharge profiles of the Zn//ZVO/Ti$_3$C$_2$T$_x$ battery at a current density of 0.5 A g^{-1}. (b) *Ex situ* XRD patterns collected at different charge/discharge depths. *Ex situ* high-resolution XPS spectroscopy of Zn 2p and V 2p at (b) point A, (c) point D and (e) point G in (a).
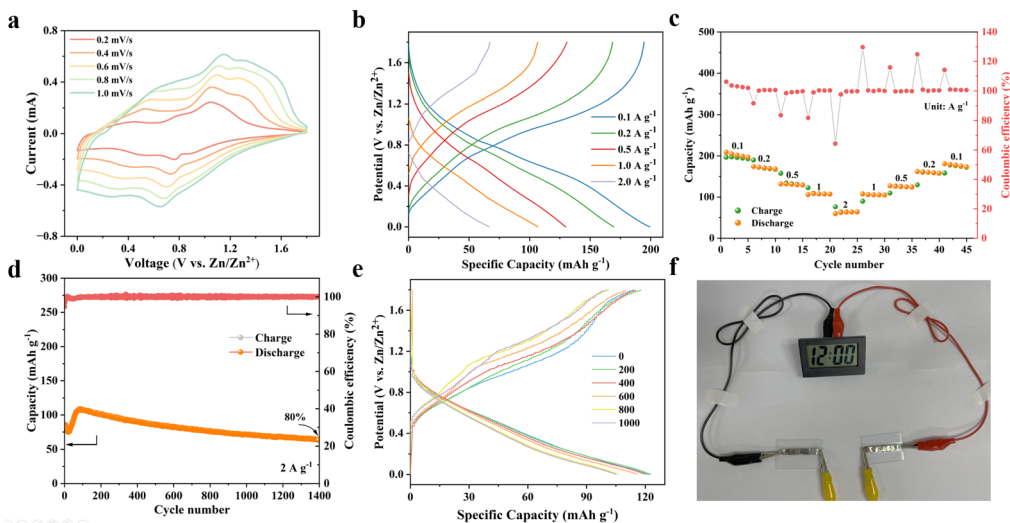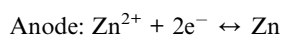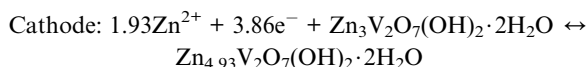
Fig. 6 (a) Cyclic voltammogram profiles of flexible Zn//ZVO/Ti$_3$C$_2$T$_x$ ZIBs at different scan rates. (b) Galvanostatic charge/discharge profiles of flexible ZIBs at a current density from 0.1 to 2.0 A g^{-1}. (c) Rate capability of flexible Zn//ZVO/Ti$_3$C$_2$T$_x$ ZIBs under different current densities. (d) Long cycling performance of flexible Zn//ZVO/Ti$_3$C$_2$T$_x$ ZIBs batteries at 2 A g^{-1}. (e) Galvanostatic charge/discharge curves of flexible Zn//ZVO/Ti$_3$C$_2$T$_x$ ZIBs during bending cycles. (f) Digital photographs of flexible Zn//ZVO/Ti$_3$C$_2$T$_x$ ZIBs in series to power a clock.

It can be calculated that 1.93 Zn^{2+} can be inserted into per molecule of ZVO at the current density of 0.1 A g^{-1}, corresponding to an ≈3.86 electron redox process. Consequently, the electrochemical reaction of the Zn//ZVO/Ti$_3$C$_2$T$_x$ battery can be illustrated and formulated as follows:

$$\text{Cathode: } 1.93Zn^{2+} + 3.86e^- + Zn_3V_2O_7(OH)_2\cdot2H_2O \leftrightarrow Zn_{4.93}V_2O_7(OH)_2\cdot2H_2O$$

$$\text{Anode: } Zn^{2+} + 2e^- \leftrightarrow Zn$$

During the discharge process, 1.93 Zn^{2+} ions were inserted into ZVO to establish the phase of Zn$_{4.93}$V$_2$O$_7$(OH)$_2$·2H$_2$O at the cathode. Meanwhile, the Zn anode was reduced to Zn^{2+}, losing the electron. Upon reverse charging, Zn^{2+} ions were gradually deserted from Zn$_{4.93}$V$_2$O$_7$(OH)$_2$·2H$_2$O to re-construct the ZVO phase, while the Zn^{2+} regained the electron to deposit on the anode.

Electrochemical performance of flexible zinc-ion batteries

Engineering flexible batteries is significant for wearable electronics. To exemplify the practicability of ZVO/Ti$_3$C$_2$T$_x$ composites, flexible ZIBs were constructed with PAM hydrogel electrolyte containing Zn^{2+} and Li$^+$ ions, a cathode of ZVO nanowires *in situ* grown on 2D Ti$_3$C$_2$T$_x$ and Zn anode, as displayed in Fig. S24.† Typical absorption bands at 1660 and 3196 cm^{-1} ascribed to C=O vibration and N–H stretching vibration, respectively, confirming the successful preparation of PAM hydrogel (Fig. S25†). Especially, PAM hydrogel possessed a 3D porous profile (Fig. S26†), which was conducive to Zn^{2+} transportation and beneficial for higher impoundment capacity. The resultant PAM hydrogel provided well-stretchable properties (a tensile strain of 1445.5% and tensile strength of

255 kPa, Fig. S27 and 28†), showing considerable deformability to the gel electrolyte of flexible ZIBs.

The CV and GCD measurements of the flexible battery at different scanning rates explored the electrochemical performance of the flexible ZIBs, as shown in Fig. 6a and b. Furthermore, the locations of the redox peak were consistent with the voltage range of the button battery (Fig. 4a). The flexible ZIBs delivered excellent rate capacities of 201.8 mAh g^{-1} at 0.1 A g^{-1} with 63.5 mAh g^{-1} at 2.0 A g^{-1}. Returning to 0.1 A g^{-1}, the discharge capacities of ZIBs retained about 88% of the initial capacity at 0.1 A g^{-1} (Fig. 6c). After 1400 cycles at 2.0 A g^{-1}, ZIBs maintained about 80% of their initial capacity with a coulomb efficiency of about 100%, indicating outstanding cycling stability (Fig. 6d). This decrease in capacity was because of the increased R_{ct} caused by the gradually generated by-products during the discharge/charge cycles, as presented in Fig. S29.† In addition, the charge/discharge curves of flexible Zn//ZVO/Ti$_3$C$_2$T$_x$ ZIBs under different bending times are shown in Fig. 6e. They exhibited about 95% capacity retention after 200 bending cycles. Moreover, after 1000 cycles of bending, ZIB-based ZVO/Ti$_3$C$_2$T$_x$ composites retained approximately 86% of their initial capacity (Fig. S30†), indicating good flexibility and showing the prospective possibility to be energy storage devices for wearable devices. Furthermore, two flexible ZIBs in series can successfully light the clock (Fig. 6f, Video S1†), proving great potential for practical applications.

Conclusions

In summary, MoS$_2$/Ti$_3$C$_2$T$_x$ composites were constructed through the 1D ZVO nanowires on 2D Ti$_3$C$_2$T$_x$ MXene by a microwave-assisted method. MXene prevented the coated ZVO from agglomerating during the intercalation/deintercalation process of Zn^{2+}, resulting in the enhanced structural stability

of ZVO/Ti$_3$C$_2$T$_x$ composites. Furthermore, the diffusion coefficient of Zn^{2+} and electrolyte-philicity of ZVO/Ti$_3$C$_2$T$_x$ composites were significantly improved. The ZVO/Ti$_3$C$_2$T$_x$ electrode exhibited ultrahigh specific discharge performance (215.2 mAh g^{-1} specific capacity at 0.1 A g^{-1}) and long cycling stability (84% capacity retention over 14 000 cycles at 10 A g^{-1}, 88% capacity retention over 1200 cycles at 2 A g^{-1}). Furthermore, the flexible Zn//ZVO/Ti$_3$C$_2$T$_x$ ZIBs using PAM gel electrolyte still delivered excellent capacities of 201.8 mAh g^{-1} at 0.1 A g^{-1} and kept 80% retention of initial capacity after 1400 cycles at 2.0 A g^{-1}. This study is expected to inspire the design of more rational cathode systems to obtain ZIBs with high capacities.

Data availability

The data supporting this article have been included as part of ESI.†

Author contributions

W. Su contributed to most experimental work. M. Lang completed the required experiments in the revised manuscript. W. Li assisted in the characterization of some materials. H. Li conceived this idea and wrote the manuscript. All the authors assisted in experiments and provided constructive comments on the text.

Conflicts of interest

There are no conflicts to declare.

Acknowledgements

References

1 B. Dunn, H. Kamath and J.-M. Tarascon, *Science*, 2011, **334**, 928–935.
2 M. Armand and J. M. Tarascon, *Nature*, 2008, **451**, 652–657.
3 M. Song, H. Tan, D. Chao and H. J. Fan, *Adv. Funct. Mater.*, 2018, **28**, 1802564.
4 J. B. Goodenough and K.-S. Park, *J. Am. Chem. Soc.*, 2013, **135**, 1167–1176.
5 Y. Li, Z. Wang, Y. Cai, M. E. Pam, Y. Yang, D. Zhang, Y. Wang and S. Huang, *Energy Environ. Mater.*, 2022, **5**, 823–851.
6 J. Ming, J. Guo, C. Xia, W. Wang and H. N. Alshareef, *Mater. Sci. Eng. R Rep.*, 2019, **135**, 58–84.
7 S. W. D. Gourley, R. Brown, B. D. Adams and D. Higgins, *Joule*, 2023, **7**, 1415–1436.
8 X. Fan, C. Zhong, J. Liu, J. Ding, Y. Deng, X. Han, L. Zhang, W. Hu, D. P. Wilkinson and J. Zhang, *Chem. Rev.*, 2022, **122**, 17155–17239.
9 G. Li, L. Sun, S. Zhang, C. Zhang, H. Jin, K. Davey, G. Liang, S. Liu, J. Mao and Z. Guo, *Adv. Funct. Mater.*, 2024, **34**, 2301291.
10 Y. Bai, Y. Qin, J. Hao, H. Zhang and C. M. Li, *Adv. Funct. Mater.*, 2024, **34**, 2310393.
11 H. Li, Y. Liu, Z. Chen, Y. Yang, T. Lv and T. Chen, *J. Colloid Interface Sci.*, 2023, **639**, 408–415.
12 X. Wang, Z. Zhang, B. Xi, W. Chen, Y. Jia, J. Feng and S. Xiong, *ACS Nano*, 2021, **15**, 9244–9272.
13 Y. Zeng, D. Luan and X. W. Lou, *Chem*, 2023, **9**, 1118–1146.
14 C. Guo, S. Yi, R. Si, B. Xi, X. An, J. Liu, J. Li and S. Xiong, *Adv. Energy Mater.*, 2022, **12**, 2202039.
15 Z. Xing, G. Xu, J. Han, G. Chen, B. Lu, S. Liang and J. Zhou, *Trends Chem.*, 2023, **5**, 380–392.
16 T. Lv, Y. Peng, G. Zhang, S. Jiang, Z. Yang, S. Yang and H. Pang, *Adv. Sci.*, 2023, **10**, 2206907.
17 L. Li, T. Jia, X. Pei, S. Hou, B. Liu, Q. Yang and Z. Zhu, *Ionics*, 2022, **28**, 283–293.
18 C. Xia, J. Guo, Y. Lei, H. Liang, C. Zhao and H. N. Alshareef, *Adv. Mater.*, 2018, **30**, 1705580.
19 H. Cao, C. Peng, Z. Zheng, Z. Lan, Q. Pan, U. G. Nielsen, P. Norby, X. Xiao and S. Mossin, *Electrochim. Acta*, 2021, **388**, 138646.
20 X. Li, X. Zhu, Z. Cao, Z. Xu, J. Shen and M. Ye, *Small*, 2022, **18**, 2105325.
21 L. Ren, G. Yu, H. Xu, W. Wang, Y. Jiang, M. Ji and S. Li, *ACS Sustain. Chem. Eng.*, 2021, **9**, 12223–12232.
22 Z. Pan, J. Yang, J. Yang, Q. Zhang, H. Zhang, X. Li, Z. Kou, Y. Zhang, H. Chen, C. Yan and J. Wang, *ACS Nano*, 2020, **14**, 842–853.
23 Y. Cui, Y. Ding, L. Guo, C. Guo, Y. Liu, Y. Bai, G. Li and K. Wang, *Energy Mater.*, 2023, **3**, 300023.
24 Y. Zhu, X. Lin, X. Jin, T. Han, H. Zhang and J. Liu, *Chem. Commun.*, 2022, **58**, 8117–8120.
25 J. Guo, J. Ming, Y. Lei, W. Zhang, C. Xia, Y. Cui and H. N. Alshareef, *ACS Energy Lett.*, 2019, **4**, 2776–2781.
26 M. Wang, G. Zhao, X. Yu, X. Bai, A. Chen, C. Zhao, P. Lyu and N. Zhang, *Nano Energy*, 2023, **110**, 108336.
27 M. Wang, G. Zhao, X. Bai, W. Yu, C. Zhao, Z. Gao, P. Lyu, Z. Chen and N. Zhang, *Adv. Energy Mater.*, 2023, **13**, 2301730.
28 P. He, M. Yan, G. Zhang, R. Sun, L. Chen, Q. An and L. Mai, *Adv. Energy Mater.*, 2017, **7**, 1601920.
29 T. Wei, Q. Li, G. Yang and C. Wang, *Electrochim. Acta*, 2018, **287**, 60–67.
30 Z. Wu, Y. Wang, L. Zhang, L. Jiang, W. Tian, C. Cai, J. Price, Q. Gu and L. Hu, *ACS Appl. Energy Mater.*, 2020, **3**, 3919–3927.
31 L. Chen, Z. Yang, J. Wu, H. Chen and J. Meng, *Electrochim. Acta*, 2020, **330**, 135347.
32 B. Lan, Z. Peng, L. Chen, C. Tang, S. Dong, C. Chen, M. Zhou, C. Chen, Q. An and P. Luo, *J. Alloys Compd.*, 2019, **787**, 9–16.
33 L. Deng, H. Chen, J. Wu, Z. Yang, Y. Rong and Z. Fu, *Ionics*, 2021, **27**, 3393–3402.
34 X. Pu, T. Song, L. Tang, Y. Tao, T. Cao, Q. Xu, H. Liu, Y. Wang and Y. Xia, *J. Power Sources*, 2019, **437**, 226917.
35 Z. Wu, C. Lu, Y. Wang, L. Zhang, L. Jiang, W. Tian, C. Cai, Q. Gu, Z. Sun and L. Hu, *Small*, 2020, **16**, 2000698.

36 H. Liu, J.-G. Wang, H. Sun, Y. Li, J. Yang, C. Wei and F. Kang, *J. Colloid Interface Sci.*, 2020, **560**, 659–666.

37 Y. Ma, Y. Qi, Y. Niu, Y. Liu, S. Bao and M. Xu, *Inorg. Chem. Front.*, 2022, **9**, 2706–2713.

38 L. Rao, Z. Zhou, H. Liu, W. Peng, Y. Li, F. Zhang and X. Fan, *J. Colloid Interface Sci.*, 2023, **629**, 473–481.

39 Y. Li, H. Ba, Z. Wang, S. Wu, Y. Shang, S. Huang and H. Y. Yang, *Mater. Today Energy*, 2024, **39**, 101460.

40 M. Liao, J. W. Wang, L. Ye, H. Sun, Y. Z. Wen, C. Wang, X. M. Sun, B. J. Wang and H. S. Peng, *Angew. Chem. Int. Ed.*, 2020, **59**, 2273–2278.

41 J. Ding, Z. Du, B. Li, L. Wang, S. Wang, Y. Gong and S. Yang, *Adv. Mater.*, 2019, **31**, 1904369.

42 N. Liu, X. Wu, L. Fan, S. Gong, Z. Guo, A. Chen, C. Zhao, Y. Mao, N. Zhang and K. Sun, *Adv. Mater.*, 2020, **32**, 1908420.

43 S. Liu, H. Zhu, B. Zhang, G. Li, H. Zhu, Y. Ren, H. Geng, Y. Yang, Q. Liu and C. C. Li, *Adv. Mater.*, 2020, **32**, 2001113.

44 W. Liang, D. Rao, T. Chen, R. Tang, J. Li and H. Jin, *Angew. Chem. Int. Ed.*, 2022, **61**, e202207779.